Laser-induced Fluorescence Measurements of Energetic Ions in a 100-A LaB_6 Hollow Cathode

Christopher A. Dodson*

University of California, Los Angeles, CA, U.S.A.

Jet Propulsion Laboratory, California Institute of Technology, Pasadena, CA, U.S.A.

Daniel Perez-Grande†

Universidad Carlos III de Madrid, Madrid, Spain

Benjamin A. Jorns‡ and Dan M. Goebel§

Jet Propulsion Laboratory, California Institute of Technology, Pasadena, CA, U.S.A.

Richard E. Wirz¶

University of California, Los Angeles, CA, U.S.A.

Increasingly long-duration space missions require a better understanding of the failure mechanisms of hollow cathodes to enable prediction of lifetime. Energetic ions have been measured in the plume of hollow cathodes but the energies are higher than can be explained classically. One of the mechanisms that appears to be contributing to the ion heating is ion acoustic turbulence (IAT), which has been investigated with plasma probes recently at JPL. In this work the ion velocity distribution has been measured using laser-induced fluorescence (LIF) at several high-current operating conditions on the centerline of a 100 A class hollow cathode at JPL. A retarding potential analyzer was (RPA) was used to measure the ion energy profile in the far plume and a Langmuir probe was used to measure electron temperature and plasma potential fluctuations. RPA energies are shown to correlate with the values measured by LIF. The ion temperature is shown to increase with distance downstream of the cathode. A parametric study of the ion heating as a function of discharge current and cathode flow rate was performed. It was found that for increasing current the ion temperature evolution did not vary even though the wave IAT wave energy increased. The effect of flow rate was more pronounced, with higher values reducing both ion temperature and wave energy linearly. These results indicate that IAT is at least partially responsible for energetic ion production in the hollow cathode plume.

Nomenclature

$\dot{m}$	= Mass flow rate
ν_{in}	= Ion-neutral collision frequency
ω	= Wave frequency
ϕ	= Plasma potential
ϕ_k	= Potential amplitude of acoustic mode with wavenumber k
c_s	= Ion acoustic speed
E	= Electric field
E_T	= Total wave energy

*Ph.D. Student, Aerospace Engineering
†Ph.D. Candidate, Aerospace Engineering
‡Research Scientist, Electric Propulsion Group, AIAA Senior Member
§Senior Research Scientist, Thermal and Propulsion Engineering Section, AIAA Fellow
¶Associate Professor, Mechanical and Aerospace Engineering, AIAA Member

f_s = Velocity distribution function of species
I_D = Discharge current
IAT = Ion acoustic turbulence
$IEDF$ = Ion energy distribution function
$IVDF$ = Ion velocity distribution function
LIF = Laser-induced fluorescence
m_s = Species mass
n_s = Species density
P_b = Chamber background pressure
q = Fundamental charge
RPA = Retarding potential analyzer
T_s = Species temperature
V_D = Discharge voltage
V_s = Species drift velocity
W_T = Wave energy density for mode with wavenumber k
z = Axial distance from the keeper face

I. Introduction

MANY long-duration space missions (up to 50 kh) have been proposed over the past two decades that would utilize ion propulsion,[1] and recently with the advent of magnetic shielding[2] Hall thrusters are now also being considered for such missions.[3,4] Hollow cathodes, which provide electrons for ionization in both thruster concepts and provide charge neutralization in ion thrusters, must also be able to meet these ambitious lifetime requirements. Recently a LaB_6 cathode designed for a 12.5 kW Hall thruster was developed to have a lifetime of as long as 75 kh when considering emitter lifetime and orifice erosion rates.[5] However, erosion of the keeper and discharge chamber of ion thrusters caused by energetic ion production in the plume still needs evaluated for these long-duration missions. Additionally, as the power of electric propulsion increases so too does the current needed from hollow cathodes. Recently a LaB_6 cathode was developed for an 80 kW Hall thruster that can sustain a current of up to 300 A.[6] However, these high currents resulted in significant erosion of the cathode keeper and orifice plate. High flow rate external gas injection was needed reduce energetic ion production sufficiently to enable >10 kh missions. The duration and cost of lifetime testing of thrusters and hollow cathodes could be much reduced if the mechanism responsible for energetic ion production could be understood and modeled. However, as of now there is still no comprehensive explanation for the mechanism by which ions gain the amount of energy measured. The objective of this work is to utilize laser-induced fluorescence (LIF) to measure the spatial evolution of the ion velocity distribution function (IVDF) in a 100 A hollow cathode plume to better understand the mechanism responsible for energetic ion production. Centerline measurements were the focus of this experimental campaign so as to compare to a 1D kinetic model that was developed.[7]

II. Previous Work

A. Erosion Observations and RPA Measurements

The initial observations of erosion of surfaces exposed to high current hollow cathode plumes was in 1988 (verify this): Rawlin[8] while testing a 10 kW xenon thruster and Brophy[9] while testing a 100-150 A cathode using either xenon or argon, which indicated the existence of a "cathode jet" of ions in both axial and radial directions. It was believed that the jet must have energies in excess of the discharge voltage to explain the erosion rates seen based on the plasma densities present and assuming the maximum ion energy to be that of the cathode-to-anode potential (<30 V). Since that time many researchers have measured the ion energy distribution function (IEDF) using retarding potential analyzers (RPA's) in hollow cathode plumes.[7,10–17] While results vary based on many factors, many of the studies show energies well in excess of the discharge voltage. Chu and Goebel[15,16] have shown that the energy content can be reduced by introducing neutral gas flow in the near plume region, which reduce the amplitude of ionization instabilities (by decreasing the ionization fraction) and ion acoustic waves (by increasing ion-neutral damping and lowering electron temperature). Ho's recent measurements of erosion of the keeper face of a 100 A LaB_6 cathode show that

erosion rates are higher than can be explained by ions falling through the sheath potential alone.[18]

B. IAT Measurements

Recent work at the NASA Jet Propulsion Laboratory (JPL) has attempted to explain the formation of these energetic ions by accounting for turbulent energy transfer in the cathode plume. Mikellides claimed that ion acoustic turbulence (IAT), caused by a high electron Mach number and electron to ion temperature ratio,[19] could exist in the cathode plume. Experiments by Jorns confirmed the existence of IAT in the plume of a hollow cathode and noted that the IAT wave energy increased increasing discharge current or decreasing flow rate.[20–22] Theoretical and experimental work by Jorns indicated that the wave energy was sufficient to cause the formation of a hot ion tail, and RPA measurements showed qualitative agreement to a 1D kinetic model ion heating on the cathode centerline.[7] However, in that study no measurements of the axial IVDF were obtained and the radial IVDF was measured only at a single location, 10 cm from the cathode centerline (compared to a plume diameter of 2 cm). While these results indicate IAT has a role in ion heating, high spatial resolution maps of the IVDF in the cathode plume are needed to validate this theory.

C. LIF Measurements

Another way to measure the IEDF is using LIF, which provides velocity information based on the measured Doppler shift of an electronic state transition in singly-charged ions. The first use of LIF on hollow cathode plumes was by Williams,[23] who investigated ion temperature and drift velocities of a low current (<20 A) cathode in both plume and spot modes of operation. Axial ion temperature generally decreased with distance downstream, the opposite of what would be expected for IAT heating. Still, he did observe ion energies in excess of the discharge voltage as well 15-20 eV ions streaming back towards the cathode at certain locations off-axis. More recent centerline LIF measurements were taken by Georgin,[24] also for low discharge currents (<20 A) using a time-resolved LIF technique. He measured a similar behavior of drift velocity as Williams but found ion temperature to increase with distance downstream up to 1 eV.

III. Experimental Setup

A. Facility

The experiments were performed at JPL's 2.6 m x 5.2 m long High Bay vacuum chamber facility, shown in Fig. 1. A Stokes Microvac/1700 Series roughing/booster pump combination is used for roughing, and a combination of LN_2 shrouds and cryogenic pumps, with a total xenon pumping speed of 40 kL/s, is used to reach a base pressure of $\sim 10^{-7}$ Torr. The facility was recently upgraded to include electrical noise isolation of low-speed diagnostics via an optical relay board by Opto-22. Control of the cathode position, power supplies, and mass flow controllers is provided by LabVIEW, as is data acquisition. Convection and ionization gauges provide pressure information. The cathode is powered by Sorensen power supplies: two DLM series for the heater and keeper, and a single DHP series for the discharge up to 330 A. Propellant flow control is provided by an Apex flow controller up to 50 sccm; calibration was performed on-site, yielding 1% error in flow rate. A needle valve on a bypass leg allows for increasing the background pressure. Research grade xenon gas was used for all testing.

B. Cathode Assembly

The testing discussed in this paper was performed using a 100 A class LaB_6 hollow cathode, shown in Fig. 2(a). Both the cathode tube and 30 mm. dia. keeper are made of PICO graphite, and the 3 mm diameter cathode orifice is made of tungsten. The 100 mm diameter, copper anode is located 30 mm downstream and aligned concentrically with the cathode. The high power capability of the cathode necessitates water cooling through a copper tube brazed onto the anode. Tungsten sheets line the inside of the anode to minimize sputtering onto the cathode. No magnetic field was used in this test series. The cathode assembly is mounted to two orthogonal stages that provide axial and lateral translation of the assembly, while probe and optical diagnostics remained fixed. Stage position is monitored via stringpots. Resistance heaters were required to prevent binding due to the low temperatures caused by the LN_2 shrouds. The entire setup is mounted at the aft end of the vacuum chamber with the anode approximately at the chamber centerline to minimize facility interactions, as shown in Fig. 2(b). The anode is biased with respect to the cathode

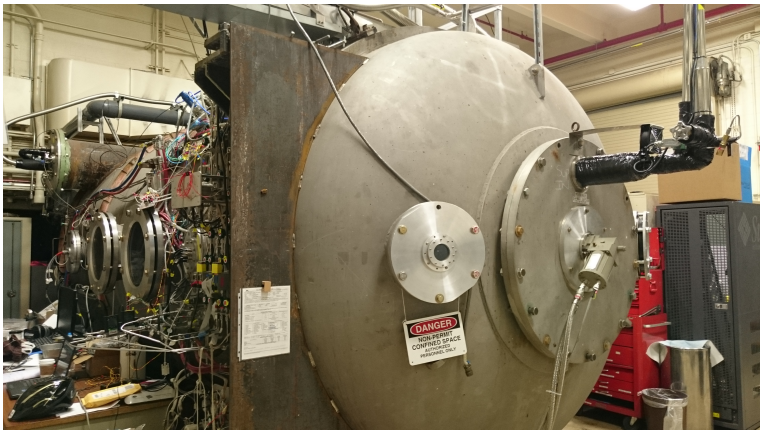

(a) Vacuum Chamber

(b) Control Rack

Figure 1: High Bay Vacuum facility

via the copper tubing which are isolated from the chamber through a non-conducting sleeve and, at the instrumentation port, through ceramic fittings. The copper tubing is connected externally to the cathode power supply in the control rack. The cathode is kept at ground potential. Both the keeper and anode float relative to the cathode.

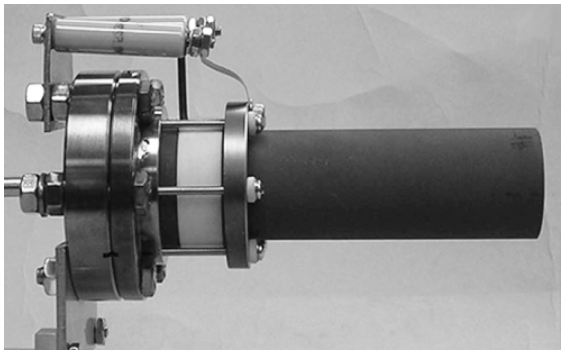

(a) 1/2" LaB_6 Hollow Cathode

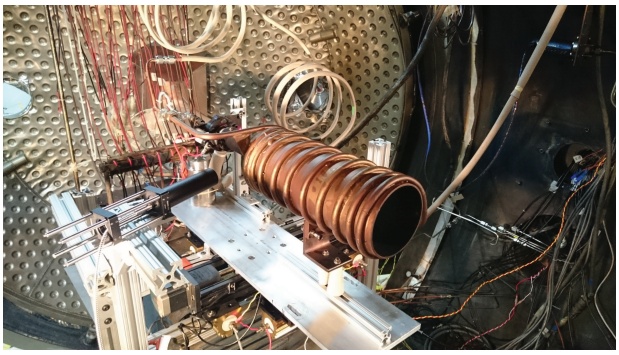

(b) Cathode Assembly

Figure 2: Cathode assembly and electrical configuration.

C. Laser Diagnostics

LIF is used to measure the Doppler shift of an absorption line of singly-ionized xenon and thereby deduce the velocity distribution. Due to its high transition probability and accessibility using easy-to-operate diode lasers, the XeII $5d^2F_{7/2} \rightarrow 6d_2^{5/2}$ transition is excited using 834.72 nm, resulting in fluorescence at 541.92 nm (both air wavelengths). LIF is preferred to an RPA because it does not perturb the plasma, measures only a single species at a time, has a high spatial resolution, and does not require knowledge of a sheath potential drop. A schematic of the laser optics table is shown in Fig. 3(a). The laser consists of a continuous-wave TLB-6700 Velocity diode seed laser coupled into a TA-7616 tapered amplifier, both by New Focus. Maximum power out is typically 550 mW. Wavelength measurement is provided by a High Finesse WS7 wavelength meter (60 MHz resolution). The injection beam is modulated at 3 kHz using an optical chopper and coupled to a 50 μm optical fiber.

Inside the chamber a 62.5 μm fiber was coupled to 25 mm injection optics that provided a 2 mm spot size at a 1 m working distance, with a maximum estimated power of 120 mW. Figure 3(b) shows optical configuration at the cathode assembly. The collection optics consist of two 25 mm dia. lenses with 75-125

mm focal lengths. The upstream-facing lens is used to observe from the keeper face to 15 mm downstream, whereas the downstream-facing lens provided access from 15-60 mm, downstream of the entrance plane of the anode. The spot sizes were 0.6-1.2 mm. The fluoresced light was focused to a 600 μm fiber which led to a Hamamatsu H10721-01 photo-multiplier tube (PMT). Wavelength filtering was provided by a bandpass filter centered at 543 nm with 22 nm FWHM acceptance. Current output from the PMT was directed to a Keithley Model 427 current amplifier, which output voltage to a Stanford Research Systems SR830 lock-in amplifier. The optical chopper was also connected to the SR830, which output the phase-sensitive detection amplified PMT signal to a LabVIEW DAQ card.

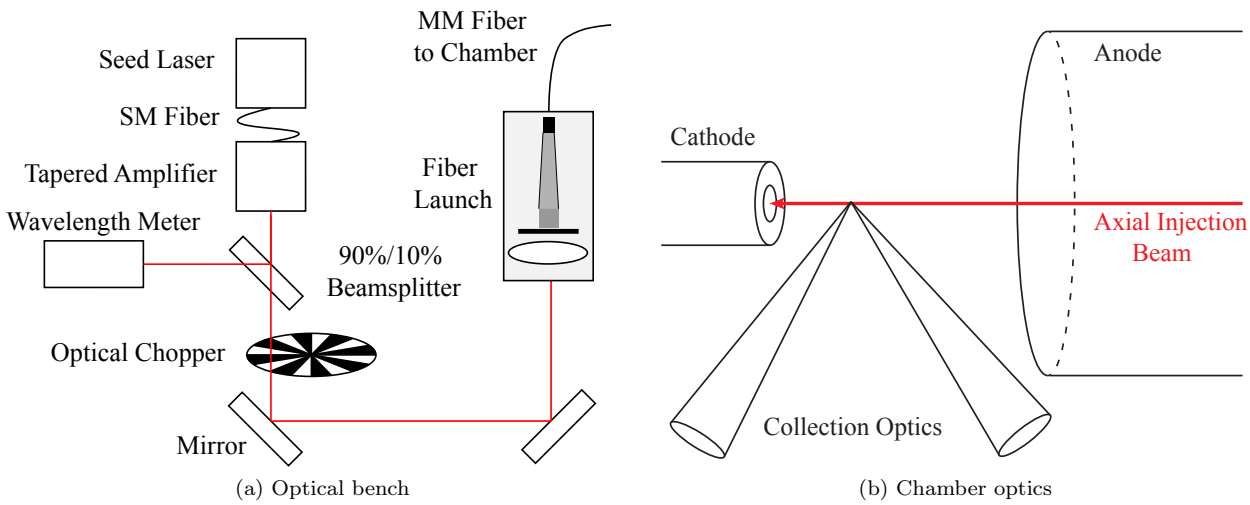

(a) Optical bench (b) Chamber optics

Figure 3: JPL cathode LIF system.

D. Probe Diagnostics

An RPA was used to measure the IEDF and a Langmuir probe was used to measure electron temperature and wave energy. This section briefly describes the operation of each as well as assumptions made in the data analysis.

1. *Retarding Potential Analyzer*

The RPA used was a four-grid type and was located on the cathode centerline at 300 mm downstream of the keeper face, approximately at the end of the anode. The first grid of the RPA was allowed to float; the second, electron-repelling grid was biased to -10 V with respect to ground; the third grid had a variable bias voltage applied to discriminate ion energies; the fourth grid was grounded through a Keithly 427 high impedance current amplifier. The output voltage from the amplifier provided a signal proportional to ion current to the collector with energies greater than the discriminator bias voltage. Because it is not possible to discern between singly- and multiply-charged ions it was assumed that singly-charged ions dominated the plasma at the RPA location. The discriminator voltage was provided by a DC power supply swept at 1 V increments from 0 to 60 V and measuring the time-averaged voltage at each step. From Sommers[17] the collector current is determined as follows:

$$I_c(V_{db}) = \frac{e^2 n_i A_c}{M_i} \int_{eV_{db}}^{\infty} f_{i,c}(E) dE, \tag{1}$$

where $I_c$is the collector current, V_{db} is the discriminator bias, e is the electron charge, n_i is ion density, A_c is collector area, M_i is the ion mass, and $f_{i,c}(E)$ is the IEDF at the collector. Differentiating, we get:

$$-\frac{dI}{dV_{db}} = \frac{e^2 n_i A_c}{m_i} f_{i,c}(E) \propto f_{i,c}(E), \tag{2}$$

where the constants were ignored since we are seeking the normalized IEDF. If the collector plate is exposed to a plasma that is at a positive potential relative to ground, ions will gain energy in falling through the sheath to the plate. To determine the IEDF in the plasma prior to the sheath, f_i, we correct for the local plasma potential, V_{pl}:

$$f_i(E) = f_{i,c}(E_c - eV_{pl}). \tag{3}$$

The value for V_{pl} at the location of the RPA was not measured in these experiments, so it was approximated to be equal to the time-averaged discharge voltage, V_d. These differentiated data were boxcar-averaged using <10 points, then normalized such that $\int_0^\infty f_i(E)dE = 1$. Because it is possible that $V_{pl} < V_d$, especially at the end of the anode, the energies calculated could be slightly higher than reported here. Also, we assume that the collector current consists primarily of singly-charged ions.

2. Langmuir Probe

The background electron temperature was measured with a 2 mm long, 0.51 mm dia. cylindrical tungsten Langmuir probe. The probe was fixed and mounted vertically. The plume location was determined by moving the cathode on its translation stages. The voltage source was a Kepco bipolar operational power supply swept from -70 V to +10 V relative to ground. The sweep was provided by a Wavetek 178 waveform synthesizer (swept at 30 Hz) isolated from the Kepco supply with an operational amplifier. Current was measured through a 50 Ω resistor by an oscilloscope, averaging the trace over 50 sweeps. The electron temperature was inferred from an exponential fit to the probe IV trace. Because of the high densities near the cathode orifice, probe measurements were taken no closer than 4 mm downstream of the keeper face. The +10 V maximum bias voltage was chosen to avoid excessive electron current (caused by densities exceeding 10^{19} m^{-3}) that could make the probe emissive. Because data was only taken over the low voltage portion of the characteristic curve it was not possible to obtain measurements of plasma potential.

3. Ion Saturation Probe

The same probe used for electron temperature was also used as an ion saturation probe by biasing it to -30 V relative to ground to measure the ion saturation current. Measurements of the upstream voltage of a 50 Ω resistor were taken with an oscilloscope, which output the power spectrum up to 3.25 MHz and the time-averaged DC voltage. The bias voltage was supplied by a battery to avoid any low-impedance paths to ground that could exist in a power supply. Following the approach of Jorns,[20] for electrostatic modes, fluctuations in plasma potential, ϕ, are related to density fluctuations as follows:

$$\phi \approx \frac{T_e}{q}\frac{\widetilde{n}_i}{\overline{n}_i}. \tag{4}$$

where $\widetilde{n}_i$ is the fluctuating ion density and $\widetilde{n}_i$ is the time-averaged ion density. If ion density is proportional to ion saturation current and if it is assumed electron temperature perturbations are small compared to density perturbations, we get the following:

$$\phi \approx \frac{T_e}{q}\frac{\widetilde{i}_{sat}}{\overline{i}_{sat}}. \tag{5}$$

We can then determine the total wave energy at each axial location, E_T, by summing the across all wavenumbers, k.

$$E_T = \sum_k \frac{[q\phi_k]^2}{T_e}. \tag{6}$$

where ϕ_k is the potential amplitude of acoustic mode with wavenumber k.

IV. Results

To evaluate the energy transferred to ions by IAT, it is desired to decouple this mechanism from others that might also add energy to the ions. Based on wave energy spectra taken in hollow cathode plumes operating at high current-to-flow rate ratios the dominant mode appears to be one that has most of its energy

content in the <100 kHz frequency range. This is generally associated with ionization instability fluctuations that can reach large amplitudes. To isolate the effects of IAT it was decided to perform measurements at currents 70 A and above. Discharge current and cathode flow rate were parametrically studied for three operating conditions each to evaluate their effect on ion heating. As was shown by Jorns,[7] the discharge voltage is correlated to IAT wave energy and, therefore, ion temperature. With this in mind, the discharge current-discharge voltage (IV) curves for this cathode were obtained prior to any other probing. This section will first discuss these IV curves for a few flow rates that provided the information leading to the decision of which conditions to test. We then will present and discuss the measurements taken both by LIF and probes along the centerline for these operating conditions.

A. Discharge Voltage Trends

IV curves obtained for 8, 10, and 15 sccm flowrates are shown in Fig. 4. It was desired to match the plasma conditions previously performed on this cathode design at JPL[7] since the plasma properties were extensively measured, so the IV curves for that study are also shown, which were taken with a background pressure of 2×10^{-4} Torr. Because of the higher pumping capacity of the current chamber a background pressure of 1×10^{-6} Torr was obtained with all pumps on. It was found that for the 8 and 10 sccm cases the lower background pressure caused a significant deviation in discharge voltage compared to the higher pressure cases, and the maximum current before strong discharge instabilities occurred was much lower. Although not shown, the IV curves for 1×10^{-5} Torr were essentially the same as the 1×10^{-6} Torr curves. To reach 2×10^{-4} Torr xenon was bled through a leak valve and only a single cryo pump was operated. The offset between the previous and current I-V curves for the higher pressure case is possibly due to the location and calibration of the ion pressure gauges used, or could be due a higher conductivity to the anode, but the overall trends are the same. All experiments reported here occurred with 2×10^{-4} Torr background pressure.

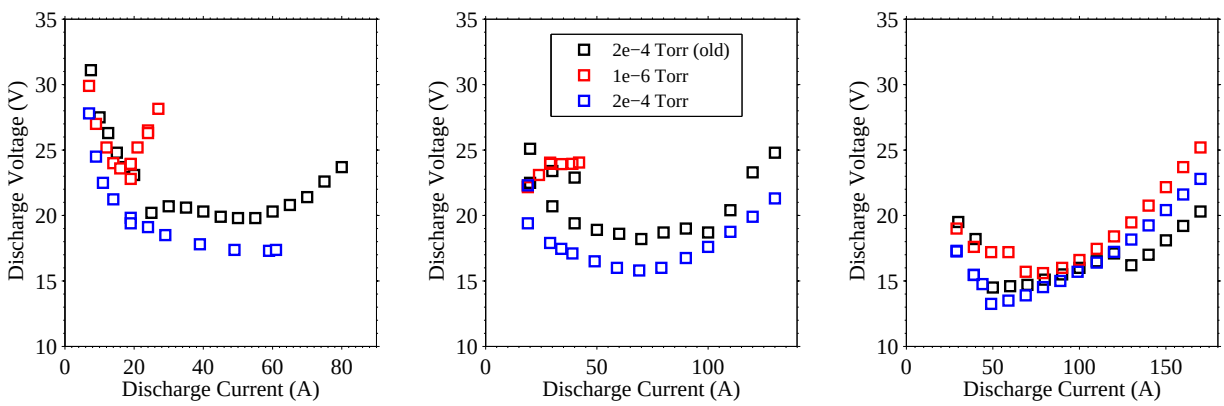

(a) 8 sccm (b) 10 sccm (c) 15 sccm

Figure 4: Discharge voltage as a function of discharge current for various flow rates and background pressures.

These results show that the overall resistivity of the discharge appears to be very sensitive to the background pressure for flowrates <15 sccm when the background pressure is below 2×10^{-4} Torr. This might be explained by the fact that anomalous resistivity is reduced as the ion-neutral collision frequency increases as it would for increasing background pressure. Likewise, with lower background pressure the resistivity and IAT wave energy increases, which could lead to more energy transfer to the ions. Although the results are not presented here, RPA measurements of the radial IEDF's showed an increase in the maximum ion energy as background pressure was reduced for a given discharge current and flow rate. Further investigation of this sensitivity to background pressure is planned, but these preliminary results underscore the importance of the neutral gas density in the cathode plume as it relates to overall resistivity and the production of energetic ions.

B. Far Plume Ion Energy Distribution

Based on the IV measurements, operating conditions for the discharge current parametric study were chosen to be 70, 100, and 130 A (at 10 sccm flow rate), and for the flow rate parametric study flow rates were chosen to be 10, 15, and 20 sccm (at 130 A discharge current). The IEDF's obtained are shown in Fig. 5(a) for variable current and Fig. 5(b) for variable flow rate. The change from 70 A to 100 A at 10 sccm produced no appreciable change to the IEDF, but increasing current to 130 A resulted in an increase in maximum energy by ∼10 eV, with the most probable energy relatively unchanged. All cases showed maximum energies greater than the ∼20 V discharge voltage. The effect of increasing flow rate at 130 A was more apparent, having the opposite effect to increasing current: the mean energy decreases as does the maximum. This makes intuitive sense based on the theory that the IAT growth rate is dampened by ion-neutral collisions, which effectively cools the ion population.

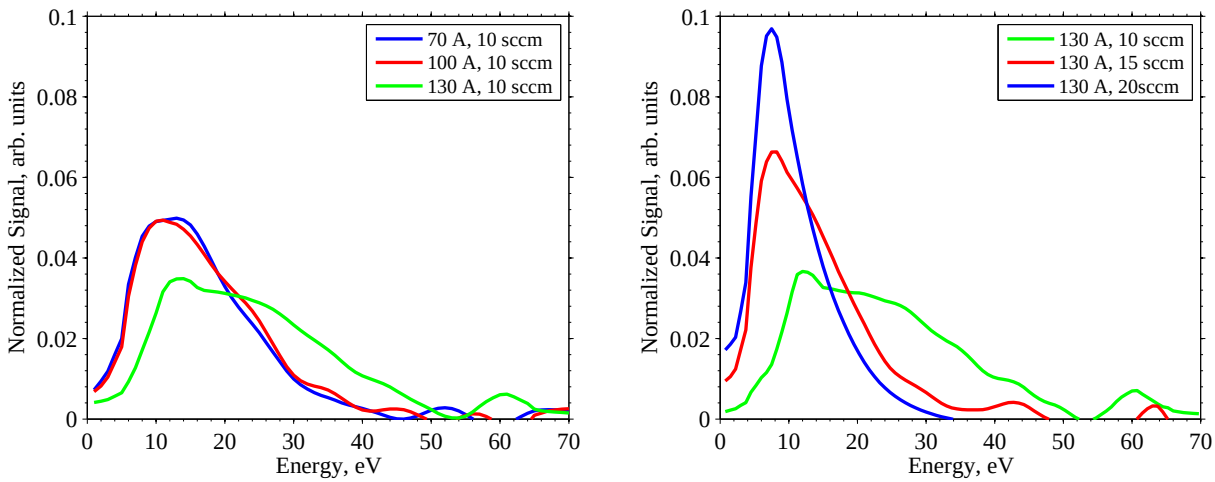

(a) Changing Current, 10 sccm

(b) Changing Flow Rate, 130 A

Figure 5: Axial ion energy distribution measurements taken by RPA. Note that the sheath potential drop has not been subtraced from these energies.

C. LIF - Data Analysis Approach

The ion velocity distribution function (IVDF) can be calculated using the using the Doppler-shift equation:

$$v_i = \frac{\Delta\nu}{\nu_0} c, \tag{7}$$

where v_i is ion velocity, $\Delta\nu$ is the difference between the laser frequency and the frequency of the absorption transition in the rest frame of the ions, ν_0, and c is the speed of light. The signal was smoothed using a boxcar averaging of <10 points and normalized such that $\int_{-\infty}^{\infty} f(v)dv = 1$. The IEDF were calculated directly from the IVDF using $E(eV) = mv^2/2e$. Finally, the primary metric of energy transfer from IAT to the ions is temperature, T_i, which we calculate as follows:

$$T_i = \frac{\frac{m_i}{k_B}\int_{-\infty}^{\infty}(v_i - v_{i,mp})^2 dv}{\int_{-\infty}^{\infty} f_i(v)dv}, \tag{8}$$

where k_B is Boltzmann's constant and $v_{i,mp}$ is the most probably ion velocity.

Figure 6 shows an example of the results obtained by LIF for the 130 A, 10 sccm operating condition. At the keeper orifice center (z = 0 mm) the IVDF is nearly Maxwellian although it is fairly hot already (>1 eV), indicating that some heating has occurred between the cathode orifice and keeper orifice since the ion temperature is estimated to be <1 eV inside the cathode orifice. The ion temperature and maximum velocity increase with distance downstream for nearly all cases tested. The degree to which this heating occurred, maximum energy, and the location of peak drift velocity varied, however, with operating condition.

Also of note is the appearance of a second, non-drifting, nearly Maxwellian ion population which begins at 15 mm downstream for this operating condition. It appeared in nearly every case evaluated but the location of its appearance and temperature also varied. This population could be interpreted as either one formed by ionization or charge-exchange collisions in the plume. Future work will attempt to identify the source of this non-drifting population.

The focus on this paper is on the heating of the drifting population since energy transfer will be higher for ions closer to the phase velocity of the ion acoustic waves and because the drifting population would result in energetic ions which is the focus of this work. The IVDF curves have been deconvolved into two Gaussian fits and all analysis is performed on the Gaussian fit to the drifting population. Note that this interpretation of the data could underestimate the ion temperature of the drifting population if in fact the non-drifting population is not Gaussian, but without knowing more about that population the extent of this uncertainty is unknown. Additionally, not all of the IVDF's could be fit well to Gaussian distributions. Evaluation of the sensitivity of the ion temperature calculations to curve fitting technique is ongoing.

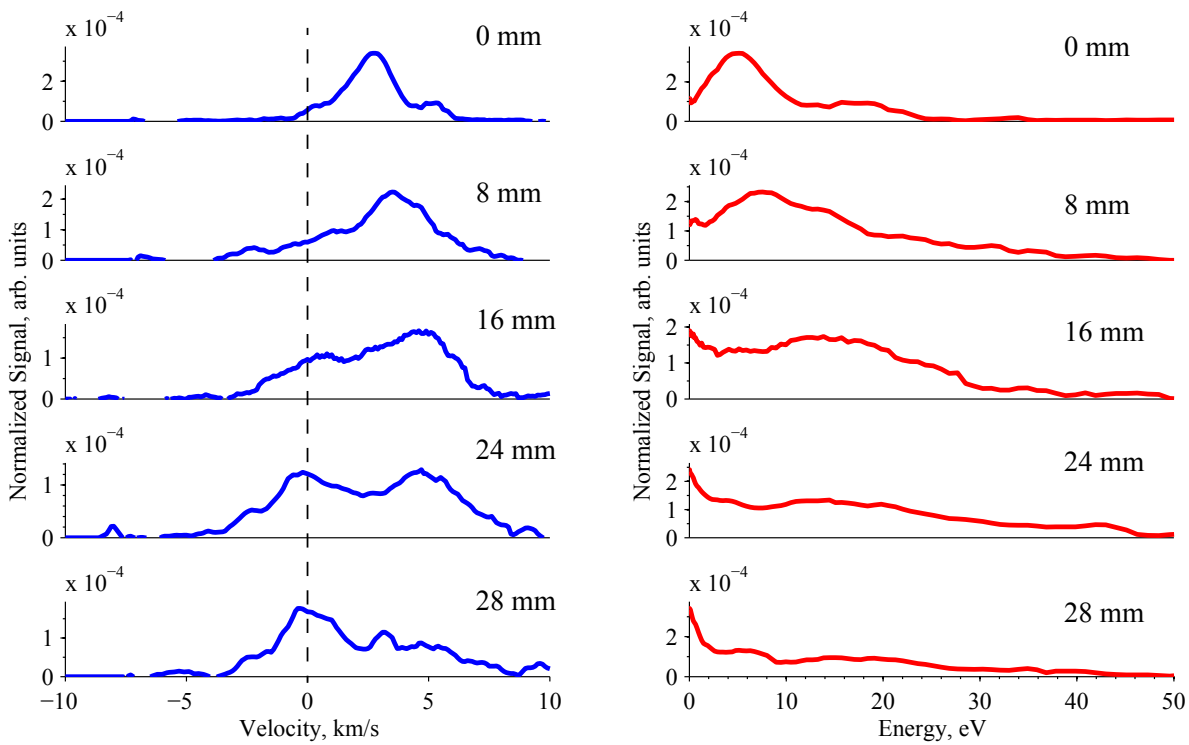

(a) Velocity Distribution

(b) Energy Distribution

Figure 6: Evolution of ion velocity and energy distributions for the 130 A, 10 sccm operating condition.

D. LIF - Energy and Temperature

To compare ion heating, Figure 7 shows the IEDF's for the two trends at 24 mm downstream of the keeper for location for all cases, since this corresponds to an IEDF that is no longer growing for all but the 130 A, 20 sccm case, which continues to grow downstream. For consistency, however, it too is evaluated at 24 mm. Figure 8 shows the same trends evaluated only for the Gaussian-fitted drifting population. Note that the Gaussian fit and raw IEDF's show similar trends, but the spreading of the IEDF is more clearly apparent. The most probably energy location is shifted slightly for the fitted data, and the maximum energy is decreased slightly, likely due to the elimination of signal at high energies corresponding to low signal-to-noise. These trends show the IEDF to be relatively insensitive to discharge current. However ion energy does seem to be sensitive to flow rate: lower flow rates have higher mean and maximum energies, and higher

flow rates have lower mean and maximum energies. This follows the same trend as the axial RPA results of IV. B, and the mean and maximum energies are similar in value using both techniques.

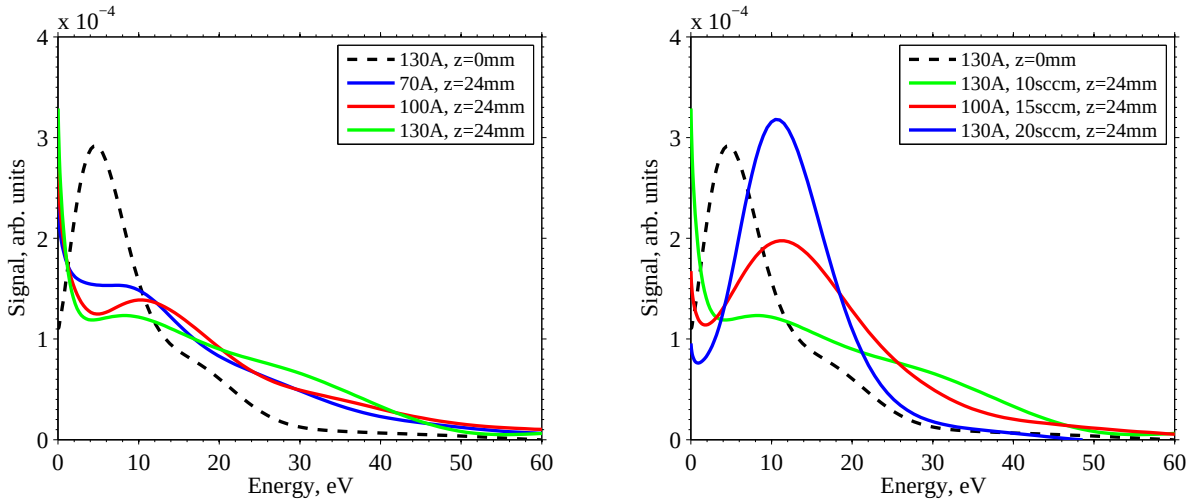

(a) IEDF's downstream for changing currents.

(b) IEDF's downstream changing flow rates.

Figure 7: IEDF at peak heating location downstream for two different trends. A representative IEDF at the orifice location is present for reference.

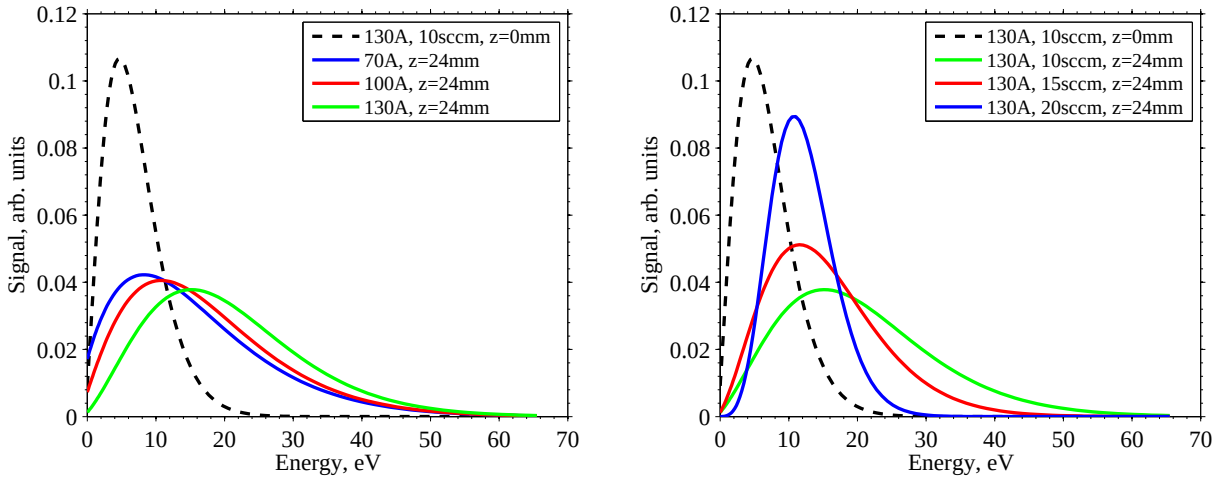

(a) IEDF's downstream for changing currents.

(b) IEDF's downstream changing flow rates.

Figure 8: IEDF at peak heating location downstream for two different trends, caluculated using Gaussian fits to the drifting population. A representative IEDF at the orifice location is present for reference.

Using Eq. 8, ion temperature was calculated for all cases and results for the two trends are shown below in Figure 9. Again we observe that ion heating is weakly dependent on current but strongly dependent on flow rate. All cases at 10 sccm show increasing temperature with distance downstream, plateauing near the anode entrance plane. It should be noted that inside the anode the signal-to-noise of the drifting population was low compared to that of the non-drifting population, making it difficult to deconvolve the two. This puts the plateau in ion temperature in question. For the case of increasing flow rate the temperature growth is suppressed and nearly flat for the 20 sccm case.

The most probably ion velocities for each case are shown in Fig. 10. All cases show an increase in drift velocity followed by a decrease past the anode entrance. Also due to questionable data quality and curve

fitting uncertainty, the values inside of the anode have large errors.

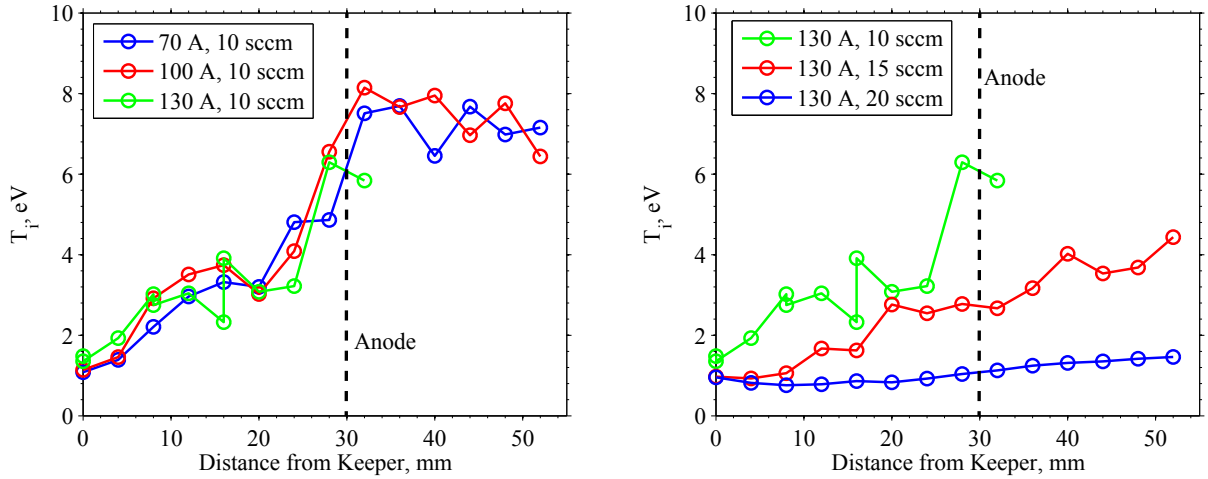

(a) Ion temperature as a function of distance downstream for varying current conditions at 10 sccm.

(b) Ion temperature as a function of distance downstream for varying current flowrates at 130 A.

Figure 9: Ion temperature as a function of distance downstream.

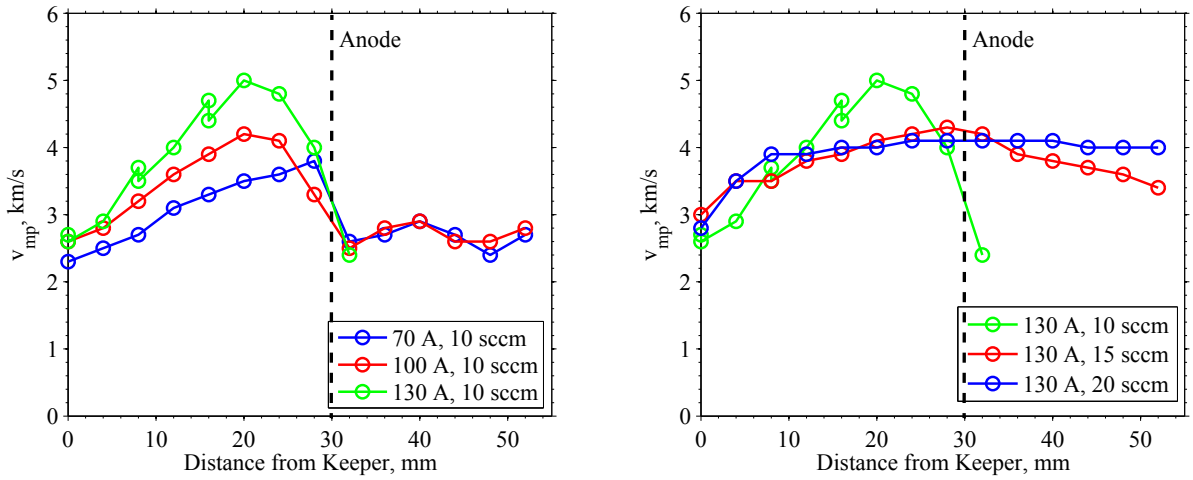

(a) v_{mp} as a function of distance downstream, for varying currents at 10 sccm.

(b) v_{mp} as a function of distance downstream, for varying flow rates at 130 A.

Figure 10: Most probable ion velocity as a function of distance downstream, assuming Gaussian curve-fit.

E. Electron Temperature

Electron temperature is needed to determine IAT wave energy per Eqs. 5 and 6. Results from Langmuir probe sweeps for the two trends are shown in Fig. 11. As found by Jorns,[7] electron temperature values between 2 and 3 eV were common generally remained constant with distance from the keeper. This consistency stems from the fact that T_e decreases with decreasing plasma density but increases with decreasing neutral gas density, both of which are occurring along the centerline with distance downstream and so the two effects nearly cancel out. T_e was found to increase with discharge current, likely due to an increase in electron-electron collision frequency, and to decrease with increasing flow rate due to depletion of electrons with sufficient energy to cause ionization.

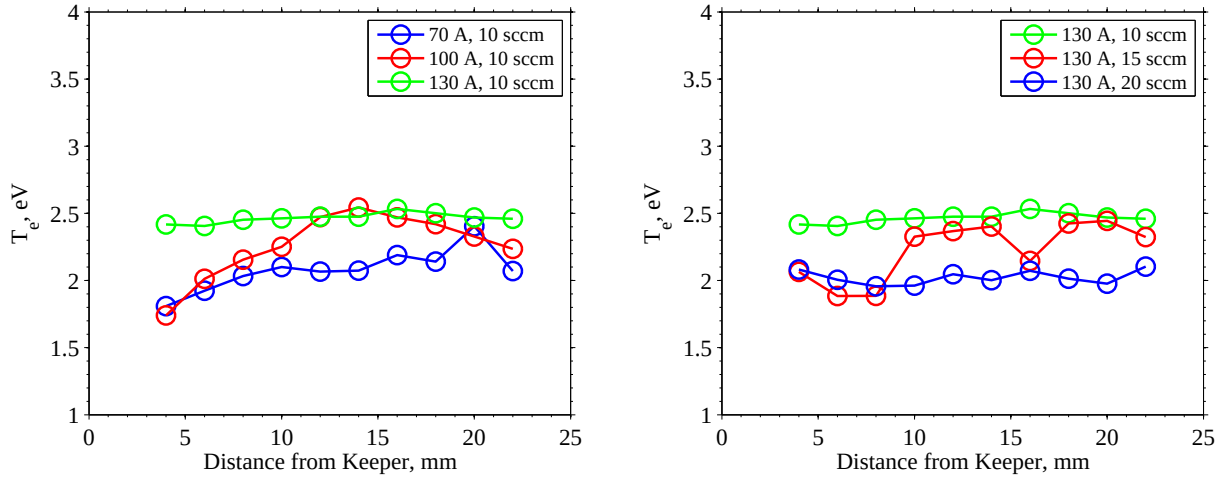

(a) Te current trend (b) Te flowrate trend

Figure 11: Electron temperature as a function of location for the five conditions studied.

F. Wave Energy

Figure 12(a) below shows a contour plot of the wave amplitude spectrum for the 70 A, 10 sccm operating condition, and Fig 12(b) shows the same for the 130 A, 10 sccm condition. Both are plotted the same scales. These show clearly the increase in wave energy due to the higher current. They both also show that high-frequency energy content associated with IAT increases with distance downstream to a maximum then gradually decreases afterwards. Figure 12(c) shows an example raw amplitude spectrum taken for the 130 A, 10 sccm operating condition, 10 mm downstream of the keeper. This plot illustrates the inverse cascade of wave energy to a maximum below 500 kHz, with decreasing energy content at both ends of the spectrum which is typical of plasma turbulence.

To make use of the wave amplitude spectra, we must calculate the total wave energy at each location and compare to the ion heating from LIF measurements. Because of the sometimes large amount of energy in the low-frequency end of the spectrum associated with ionization instabilities (which we want to ignore here), a cutoff of 100 kHz was used above which the wave amplitude is integrated. The wave energies for the two trends are shown in Fig. 13. They show similar results to the ion temperature measurements: increasing current for a given flow rate increases the wave energy and moves the location of peak wave energy upstream, with similar trends for decreasing flow rate.

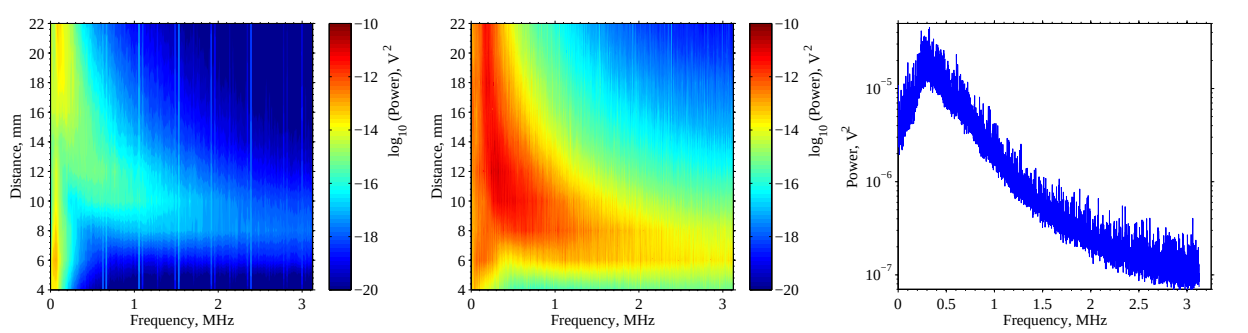

(a) 70 A, 10 sccm (b) 130 A, 10 sccm (c) 130 A, 10 sccm, 10 mm downstream

Figure 12: Amplitude spectrum for 70 A and 130 A, 10 sccm cases, with an example of the raw amplitude spectrum.

To more clearly illustrate the correlation of ion temperature with IAT wave energy, Figure 14 shows both

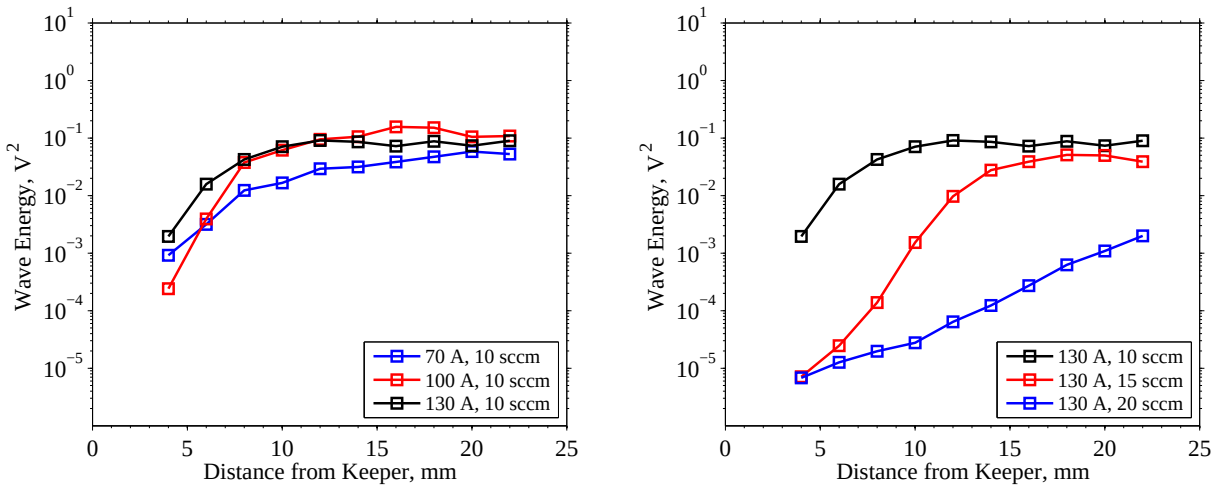

(a) Changing Current, 10 sccm

(b) Changing Flow Rate, 130 A

Figure 13: Wave energy for the two trends.

with respect to distance downstream of the keeper for each operating condition, all to the same scale. Note that since the ions havea finite temperature at the keeper orifice this temperature was subtracted tocompare explicitly to wave energy available for heating. These plots show that for the three cases at 130 A there is a linear relationship between T_i and E_T. However, as discussed above, this is not true for the 70 and 100 A cases.

V. Conclusion

This work has provided useful data on the evolution of the IVDF in the near plume of a high current hollow cathode at current levels not before probed using LIF. The correlations of IEDF data between LIF and RPA follow similar trends and, for the most part, result in similar maximum ion energies. The IEDF profiles, ion temperature calculations, and wave energy measurements all appear much more sensitive to flow rate than discharge current at the conditions examined. Why this is the case remains for future investigation. Also unknown is why the ion temperature does not scale linearly with wave energy for the 70 and 100 A (both 10 sccm) operating conditions as it does for all three 130 A conditions. Possible causes include curve-fitting techniques or the assumptions used in calculating wave energy. However, the parametric study of flow rate shows clear, intuitive trends. Perhaps a more appropriate choice of operating conditions will shed light on discharge current sensitivity. Another result from this work was to show the sensitivity of the overall plasma resistivity to background pressures below 2×10^4 Torr. This could be important in the life-testing of hollow cathodes in which erosion from energetic ion production is being evaluated.

Future work planned includes the following: performing 2D maps with LIF and the probes used in this study, as well as a 2D wave vector probe, for several operating conditions; comparing the results of this study to a 1D model for IVDF evolution on the centerline; and taking centerline measurements of a 300 A cathode to better understand the dependence of energetic ion production on discharge current. These results should improve our understanding of energetic ion production and will be valuable for validating models in development at JPL that seek to self-consistently predict IAT-driven anomalous resistivity and energetic ion production in hollow cathode plumes.[25]

Acknowledgments

The research described in this paper was carried out at the Jet Propulsion Laboratory, California Institute of Technology, under a contract with the National Aeronautics and Space Administration and funded through the Advanced In-Space Propulsion Technologies program. The authors would like to acknowledge Ray

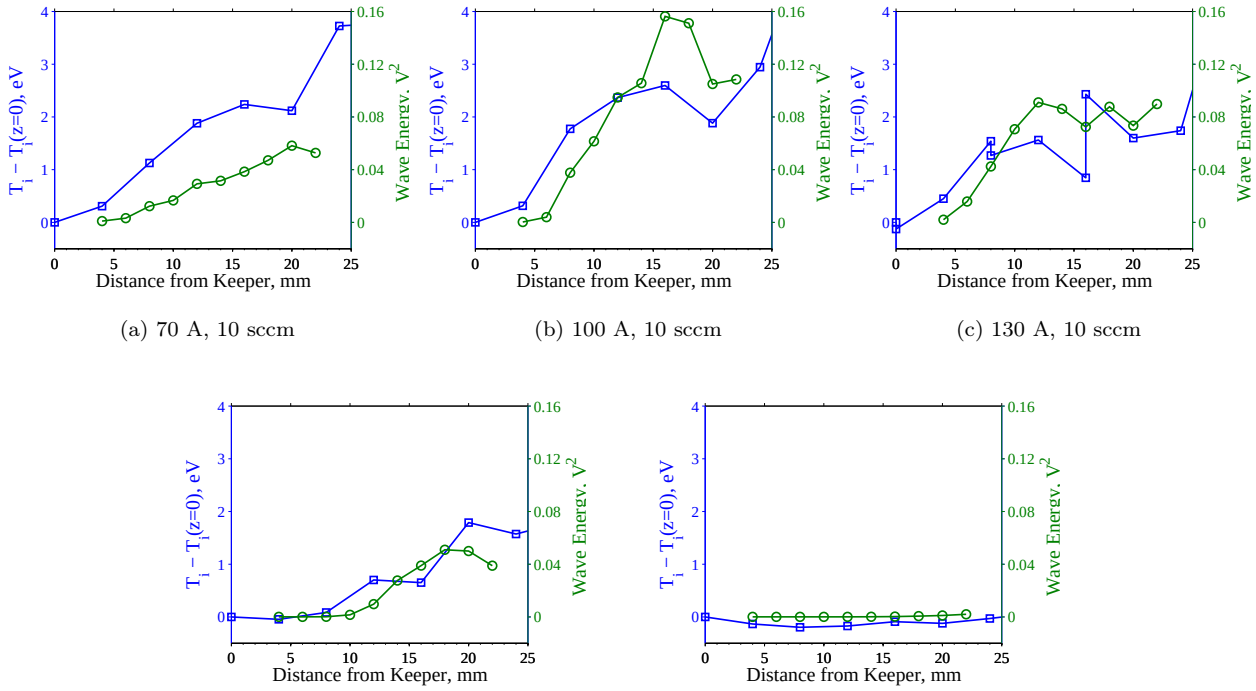

(a) 70 A, 10 sccm

(b) 100 A, 10 sccm

(c) 130 A, 10 sccm

(d) 130 A, 15 sccm

(e) 130 A, 20 sccm

Figure 14: Ion temperature and wave energy as functions of axial location for each operation condition.

Swindlehurst and Nowell Niblitt for their assistance in running the experimental facility.

References

[1]Polk, J., "An Overview of the Nuclear Electric Xenon Ion System (NEXIS) Program," *39th AIAA/ASME/SAE/ASEE Joint Propulsion Conference and Exhibit*, , No. July, 2003, pp. 1–20.

[2]Mikellides, I. G., Katz, I., Hofer, R. R., and Goebel, D. M., "Magnetic Shielding of the Acceleration Channel Walls in a Long-Life Hall Thruster," *AIAA*, , No. July, 2010, pp. 1–25.

[3]Kamhawi, H., Huang, W., Haag, T., Yim, J., Chang, L., Clayman, L., Herman, D., Shastry, R., Thomas, R., Griffith, C., Myers, J., Williams, G., Mikellides, I. G., Hofer, R., Polk, J. E., and Goebel, D. M., "Overview of the Development of the Solar Electric Propulsion Technology Demonstration Mission 12.5 kW Hall Thruster," *The 50th AIAA/ASME/SAE/ASEE Joint Propulsion Conference & Exhibit*, , No. 353, 2014, pp. 2014–3898.

[4]Hofer, R. R., Kamhawi, H., Herman, D., Polk, J. E., Snyder, J. S., Mikellides, I., Huang, W., Myers, J., Yim, J., Williams, G., Ortega, A. L., Jorns, B., Sekerak, M., Griffiths, C., Shastry, R., Haag, T., Verhey, T., Gilliam, B., Katz, I., Goebel, D. M., Anderson, J. R., Gilland, J., and Clayman, L., "Development Approach and Status of the 12.5 kW HERMeS Hall Thruster for the Solar Electric Propulsion Technology Demonstration Mission," *34th International Electric Propulsion Conference*, 2015, pp. IEPC–2015–186.

[5]Goebel, D. M. and Polk, J. E., "Lanthanum Hexaboride Hollow Cathode for the Asteroid Redirect Robotic Mission 12.5 kW Hall Thruster," *34th International Electric Propulsion Conference*, 2015, pp. IEPC–2015–43.

[6]Goebel, D. M. and Chu, E., "High Current Lanthanum Hexaboride Hollow Cathode 20-to-100 kW Class Hall Thrusters," *Journal of Propulsion and Power*, Vol. 30, No. Jan-Feb, 2014, pp. 30–40.

[7]Jorns, B. A., Mikellides, I. G., Goebel, D. M., and Ortega, A. L., "Mitigation of energetic ions and keeper erosion in a high-current hollow cathode," 2015.

[8]Rawlin, V. K., "Internal Erosion Rates of a 10-kW Xenon Ion Thruster AIAA-88-2912," 1988.

[9]Brophy, J. R. and Garner, C. E., "AIAA-88-2913 TESTS OF HIGH CURRENT HOLLOW CATHODES FOR ION ENGINES Pasadena , CA AIAA / ASME / SAE / ASEE 24th JOINT PROPULSION CONFERENCE," 1988.

[10]Friedly, V. and Wilbur, P., "High Current Hollow Cathode Phenomena," *21st International Electric Propulsion Conference*, Vol. 8, No. 3, 1990, pp. 635–643.

[11]Friedly, V., "Hollow cathode operation at high discharge currents," Tech. rep.

[12]Foster, J. E. and Patterson, M. J., "Plasma Emission Characteristics from a High Current Hollow Cathode in an Ion Thruster Discharge Chamber," , No. July, 2002, pp. 1–17.

[13]Goebel, D. M., Jameson, K. K., Katz, I., and Mikellides, I. G., "Potential fluctuations and energetic ion production in hollow cathode discharges," *Physics of Plasmas*, Vol. 14, No. 10, 2007, pp. 103508.

[14]Farnell, C., *Plasma flow field measurements downstream of a hollow cathode*, Ph.D. thesis, 2008.

[15]Chu, E., "External Mass Injection to Reduce Energetic Ion Production in the Discharge Plume of High Current Hollow Cathodes," 2012.

[16]Chu, E., Goebel, D. M., and Wirz, R. E., "Reduction of Energetic Ion Production in Hollow Cathodes by External Gas Injection," *Journal of Propulsion and Power*, Vol. 29, No. 5, 2013, pp. 1155–1163.

[17]Sommers, B. S., Foster, J. E., Davis, C. N., and Viges, E., "Preliminary Characterization of Ion Energy Spectra Acquired from High Current Hollow Cathodes," *Iepc*, 2013, pp. 1–10.

[18]Williams, G., Smith, T., Domonkos, M., Gallimore, A., and Drake, R., "Laser-induced fluorescence characterization of ions emitted from hollow cathodes," *IEEE Transactions on Plasma Science*, Vol. 28, No. 5, 2000, pp. 1664–1675.

[19]Mikellides, I. G., Katz, I., Goebel, D. M., and Jameson, K. K., "Evidence of nonclassical plasma transport in hollow cathodes for electric propulsion," *Journal of Applied Physics*, Vol. 101, No. 6, 2007, pp. 063301.

[20]Jorns, B. A., Mikellides, I. G., and Goebel, D. M., "Temporal Fluctuations in a 100-A LaB6 Hollow Cathode," *33rd International Electric Propulsion Conference*, 2013, pp. IEPC–2013–385.

[21]Jorns, B. a., Mikellides, I. G., and Goebel, D. M., "Ion acoustic turbulence in a 100-A LaB 6 hollow cathode," *Physical Review E*, Vol. 90, No. 6, 2014, pp. 1–10.

[22]Jorns, B., Goebel, D. M., and Mikellides, I. G., "Investigation of Energetic Ions in a 100-A Hollow Cathode," *50th AIAA/ASME/SAE/ASEE Joint Propulsion Conference*, 2014, pp. 1–17.

[23]Williams, G., Smith, T., Domonkos, M., Gallimore, A., and Drake, R., "Laser-induced fluorescence characterization of ions emitted from hollow cathodes," *IEEE Transactions on Plasma Science*, Vol. 28, No. 5, 2000, pp. 1664–1675.

[24]Georgin, M., Durot, C., and Gallimore, A. D., "Preliminary Measurements of Time Resolved Ion Velocity Distributions Near a Hollow Cathode," 2015, pp. 1–15.

[25]Ortega, A. L., Mikellides, I. G., and Jorns, B. A., "First-principles Modeling of IAT-driven Anomalous Resistivity in Hollow Cathode Discharges II: Numerical Simulations and Comparisons with Experiments," *52nd AIAA/SAE/ASEE Joint Propulsion Conference*, 2016.